Available online at www.sciencedirect.com
ScienceDirect
Nuclear Instruments and Methods in Physics Research A 592 (2008) 16–25
NUCLEAR INSTRUMENTS & METHODS IN PHYSICS RESEARCH Section A
www.elsevier.com/locate/nima

Simulations of radiation-damaged 3D detectors for the Super-LHC

D. Pennicard[a,*,1], G. Pellegrini[b], C. Fleta[a], R. Bates[a], V. O'Shea[a], C. Parkes[a], N. Tartoni[c]

[a]Department of Physics and Astronomy, University of Glasgow, Kelvin Building, University Avenue, Glasgow G12 8QQ, UK
[b]Instituto de Microelectronica de Barcelona, IMB-CNM-CSIC, 08193 Bellaterra, Barcelona, Spain
[c]Diamond Light Source Ltd., Harwell Science and Innovation Campus, Oxfordshire OX11 0DE, UK

Received 14 January 2008; received in revised form 20 March 2008; accepted 24 March 2008
Available online 27 March 2008

Abstract

Future high-luminosity colliders, such as the Super-LHC at CERN, will require pixel detectors capable of withstanding extremely high radiation damage. In this article, the performances of various 3D detector structures are simulated with up to 1×10^{16} 1 MeV-n_{eq}/cm^2 radiation damage. The simulations show that 3D detectors have higher collection efficiency and lower depletion voltages than planar detectors due to their small electrode spacing.

When designing a 3D detector with a large pixel size, such as an ATLAS sensor, different electrode column layouts are possible. Using a small number of n+ readout electrodes per pixel leads to higher depletion voltages and lower collection efficiency, due to the larger electrode spacing. Conversely, using more electrodes increases both the insensitive volume occupied by the electrode columns and the capacitive noise. Overall, the best performance after 1×10^{16} 1 MeV-n_{eq}/cm^2 damage is achieved by using 4–6 n+ electrodes per pixel.

PACS: 29.40.Gx; 29.40.Wk; 85.30.De

Keywords: 3D detectors; Radiation hardness; Device simulation; LHC; ATLAS; Pixel detector

1. Introduction

The Large Hadron Collider (LHC) at CERN [1] will be used to explore particle physics at the TeV scale. Its main aims will be to search for the Higgs particle, to search for other new physics such as supersymmetry, and to make more accurate measurements of Standard Model parameters such as the masses of the W bosons and the top quark. Although the LHC has not yet begun to operate, there are already plans for an upgrade to the collider, referred to as "Super LHC" (SLHC) [2]. This upgrade would increase the luminosity of the collider by a factor of 10, giving a 10-fold increase in the number of collisions produced. This would improve the chances of discovering new high-energy particles, giving a 20–30% increase in the LHC's mass reach, and also allow more precise measurements of (for example) the parameters of the Higgs. However, the increase in the number of collisions would also put greater demands on the detectors used in the experiments.

ATLAS, a general-purpose experiment at the LHC, uses a silicon pixel detector close to the collision point [3]. The pixel detector is important for accurately reconstructing the paths of particles produced by the collisions. Due to its closeness to the collision point, the pixel detector receives a lot of radiation damage; the innermost layer of the detector, the b-layer, will need to be replaced after about 3 years of operation at the LHC's design luminosity. The proposed SLHC upgrade would increase the damage by a factor of 10. The b-layer, about 5 cm from the beamline, would then receive an equivalent fluence of about 1×10^{16} 1 MeV-n_{eq}/cm^2 over the SLHC's running time, mostly in the form of charged hadrons [4]. So, the pixel detector for the SLHC would need to be much more radiation-hard than the present one.

The 3D detector architecture, proposed by Parker et al. [5], is a promising option for both the b-layer replacement

*Corresponding author. Tel.: +44 141 330 5893.
E-mail address: d.pennicard@physics.gla.ac.uk (D. Pennicard).
[1]Supported by the UK Engineering and Physical Sciences Research Council, and by Diamond Light Source PLC.

0168-9002/$ - see front matter © 2008 Elsevier B.V. All rights reserved.
doi:10.1016/j.nima.2008.03.100

and the SLHC [6]. Whereas standard pixel detectors have planar electrodes on their front and back surfaces, 3D detectors use arrays of n- and p-type columns passing through the thickness of a silicon substrate. This means that a 3D detector can combine a reasonably thick substrate with a much smaller spacing between n- and p-electrodes. (When using 10 μm-diameter columns, the maximum column depth that can be achieved using current etching methods is about 250 μm.) This improves the detectors' radiation hardness in two ways. Firstly, some of the defects created by radiation damage can act as acceptors. As the substrate's effective doping concentration increases, its depletion voltage gets very large. In n-type substrates, type inversion also occurs [7]. Because 3D detectors only have to be depleted a short distance from one electrode to the next, they have substantially lower depletion voltages. Secondly, radiation-induced defects can trap the free electrons and holes produced by an incident particle, preventing them from being collected and reducing the readout signal. The effects of trapping can be lessened by collecting the charges as quickly as possible. The small electrode spacing in a 3D detector means that the carriers' drift distance, and hence their collection time, is greatly reduced.

It can be helpful to model the behaviour of new detectors using computer simulation, in order to understand their behaviour better and to optimise their design. While other papers have looked at the behaviour of 3D detectors before irradiation [5,8,9], this paper investigates their performance following SLHC levels of radiation damage, up to a fluence of 1×10^{16} 1 MeV-n_{eq}/cm^2. In particular, this paper focuses on evaluating the performance of different possible ATLAS 3D pixel devices.

Although it is possible to use either the n+ or the p+ columns in a 3D detector for readout, the ATLAS pixel readout chip [3] is designed to use n+ readout, so this has been used in all of the simulations for the sake of consistency. Similarly, although it is possible to use n+ readout in devices with n-type substrates, using a p-type substrate has the advantage that type inversion does not take place. So, all the simulations have used the same p-type radiation-damage model.

2. Simulation methods, and comparison with experimental results from planar detectors

2.1. Synopsys TCAD

All of the following simulations were done with "Synopsys TCAD" version Z-2007.03 [10], a finite-element semiconductor simulation package. This package approximates the structure of the simulated device as a 3D "mesh" of discrete elements. By applying the appropriate semiconductor equations and boundary conditions to the mesh, the behaviour of the device can be simulated under different conditions [11]. Refs. [9,12] provide further discussion of this package.

The simulation applies reflecting (Neumann) conditions at the boundaries of the device mesh, i.e., the electric field and current density normal to the boundary are zero. The simulation will be accurate if the mesh boundaries correspond to planes of symmetry in the real device, where these conditions will apply. Since these 3D devices have very symmetrical structures, it was often possible to accurately determine their behaviour using just a small region of the device, thus reducing the complexity of the mesh and allowing the simulations to run more quickly. The outer surfaces of the oxide layers also used Neumann conditions. This is a good approximation to the oxide behaviour in a "clean" wafer [13].

2.2. Radiation-damage model

When high-energy particles such as hadrons pass through a detector, they collide with silicon atoms and displace them from their lattice sites, resulting in pairs of interstitial atoms and vacancies. These defects may recombine, or they may form complexes with each other or with existing impurities in the silicon [14]. These defects introduce extra energy levels within the bandgap of the silicon. Synopsys simulates this bulk radiation damage by directly modelling the dynamics of these traps [10,15]. So, the user has to provide Synopsys with the concentrations and parameters of the traps.

The trap levels used here are designed to model p-type float zone silicon following proton irradiation, and are based on work done at the University of Perugia [16]. The details of the traps are given in Table 1. The traps are parametrised by their type, their energy level, the associated defect, and their electron and hole cross-sections σ_e, σ_h (which reflect the probability of trapping free carriers). The trap concentrations increase linearly with fluence, as given by the introduction rate η. Some of the carrier cross-sections which were used in Ref. [16] have been changed, as explained later; the changes are marked by asterisks.

When the device is depleted, the traps will have various effects. The two acceptor levels are slightly above the middle of the bandgap. Firstly, due to their proximity to the midgap, the acceptors will generate electron–hole pairs, increasing the leakage current. Although most of the acceptors will be empty, a small proportion will be occupied by electrons and become negatively charged, increasing the effective p-type doping. Thirdly, the unoccupied acceptors will trap excess electrons from the conduction

Table 1
p-Type float zone silicon trap model, based on Ref. [16]

Type	Energy (eV)	Defect	σ_e (cm^2)	σ_h (cm^2)	η (cm^{-1})
Acceptor	$E_C - 0.42$	VV	$*9.5 \times 10^{-15}$	$*9.5 \times 10^{-14}$	1.613
Acceptor	$E_C - 0.46$	VVV	5.0×10^{-15}	5.0×10^{-14}	0.9
Donor	$E_V + 0.36$	C_iO_i	$*3.23 \times 10^{-13}$	$*3.23 \times 10^{-14}$	0.9

Asterisks indicate the values that have been changed.

band. The third level is a donor, and is further from the midgap. Its main effect will be to trap excess holes from the valence band.

The original trap model in Ref. [16] can accurately model the increase in leakage current and effective doping concentration (N_{eff}) due to radiation damage. Experimentally, the change in N_{eff} varies depending on the impurities present in the silicon; this model was specifically chosen to match float zone. In this paper, the carrier cross-sections have been modified in order to accurately model the trapping rates. The effective doping concentration will not be significantly affected, but the accuracy of the leakage current will be reduced somewhat.

When excess electrons are generated in silicon, the rate of electron trapping, R_{e}, is given by

$$R_{\mathrm{e}} = \frac{n}{\tau_{\mathrm{eff_e}}} \tag{1}$$

where $\tau_{\mathrm{eff_e}}$ is the effective electron lifetime and n is the electron concentration. Experimentally, the inverse of the lifetime increases linearly with the radiation fluence Φ_{eq}, and can be parametrised by

$$\frac{1}{\tau_{\mathrm{eff_e}}} = \beta_{\mathrm{e}}\Phi_{\mathrm{eq}}. \tag{2}$$

Then, looking at the trap dynamics, the parameter β_{e} is related to the trap parameters by

$$\beta_{\mathrm{e}} = \sum v_{\mathrm{th}}^{\mathrm{e}}\sigma_{\mathrm{e}}\eta \tag{3}$$

where $v_{\mathrm{th}}^{\mathrm{e}}$ is the electron thermal velocity. The summation is done over all the traps above the midgap because these traps will nearly all be empty, whereas those below the midgap will nearly all be occupied by electrons. Similar equations apply to hole trapping [17]. Ultimately, this means the trapping rate can be altered by adjusting the traps' cross-sections. It can also be shown that as long as $\sigma_{\mathrm{e}}/\sigma_{\mathrm{h}}$ is kept constant, the effective doping concentration will be altered very little.

In this model, the cross-sections have been chosen to reproduce experimental values of $\beta_{\mathrm{e,h}}$ following irradiation from Ref. [18]. These are $\beta_{\mathrm{e}} = 4.0 \times 10^{-7}\,\mathrm{cm^2\,s^{-1}}$ and $\beta_{\mathrm{h}} = 4.4 \times 10^{-7}\,\mathrm{cm^2\,s^{-1}}$.

An important point here is that the data on trapping times is only available for fluences below $1 \times 10^{15}\,\mathrm{n_{eq}/cm^2}$. This is because the "charge correction" method used to measure the lifetimes will only work with fully depleted detectors, and at high fluences a detector's depletion voltage becomes very large. So, this model works on the assumption that the linear relationship between fluence and trapping in Eq. (2) can be *extrapolated* all the way up to $1 \times 10^{16}\,\mathrm{n_{eq}/cm^2}$.

Since the behaviour of the traps is affected by the width of the bandgap, all the simulations were done using the same bandgap model—Slotboom [19]. These trap models were designed to work using Synopsys TCAD's default temperature setting of 300 K, whereas during lab tests a detector may operate at "room temperature" or be cooled to 263 K or so depending on the particular test setup. (When they are not being tested, detectors are stored at low temperatures to prevent unwanted annealing.) Experimentally, the leakage current generated by the traps increases predictably with temperature, and leakage current values are normally scaled to 293 K to allow a fair comparison [7].

Finally, to model the effects of surface damage, a layer of uniform positive charge was introduced at the interface between the silicon substrate and the oxide layer. This had an area density of $4 \times 10^{11}\,\mathrm{cm^{-2}}$ before irradiation, and $1 \times 10^{12}\,\mathrm{cm^{-2}}$ after irradiation [16].

2.3. Comparing the damage model to experiment

Next, this radiation-damage model was applied to planar detectors, to check that it gives accurate results. Firstly, a 280 μm-thick n-in-p pad detector was simulated with different damage fluences, to determine the variation in depletion voltage and leakage current. The structure and substrate doping of these devices matched those tested in Ref. [20]. The resulting depletion voltages in Fig. 1 show a good match between the simulation and experiment.

The leakage current after irradiation is parametrised by $I_{\mathrm{leak}}/\mathrm{Vol} = \alpha\Phi_{\mathrm{eq}}$. The simulation gives $\alpha = 5.13 \times 10^{-17}\,\mathrm{A\,cm^{-1}}$, whereas the experimental value is $\alpha = (3.99 \pm 0.03) \times 10^{-17}\,\mathrm{A\,cm^{-1}}$, measured at 293 K following an 80 min anneal at 60 °C [21]. So, the simulated value is about 30% higher than experiment. Given that these simulations are intended to model N_{eff} and trapping rather than leakage current, and the experimental value of the leakage current can change by more than 30% under different annealing conditions, this result is acceptable.

Next, the charge collection behaviour of a 280 μm-thick n-in-p strip detector was simulated. This was done by

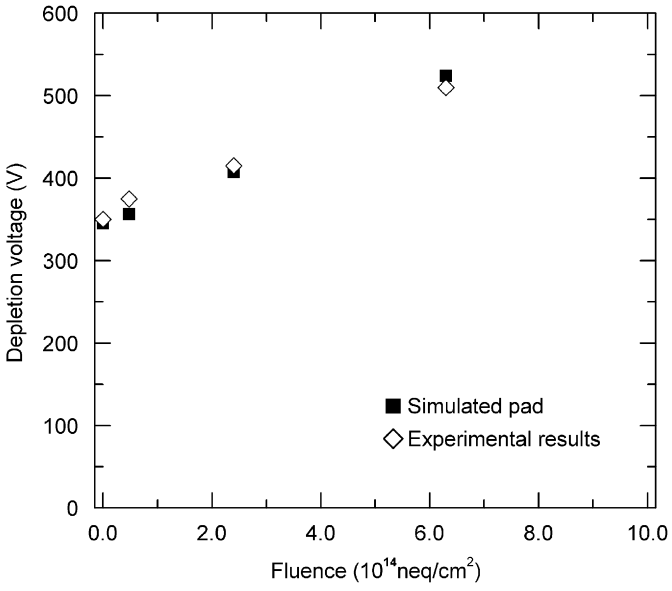

Fig. 1. Comparison between simulated and experimental depletion voltages in n-in-p pad detectors. Experimental results are taken from Ref. [20].

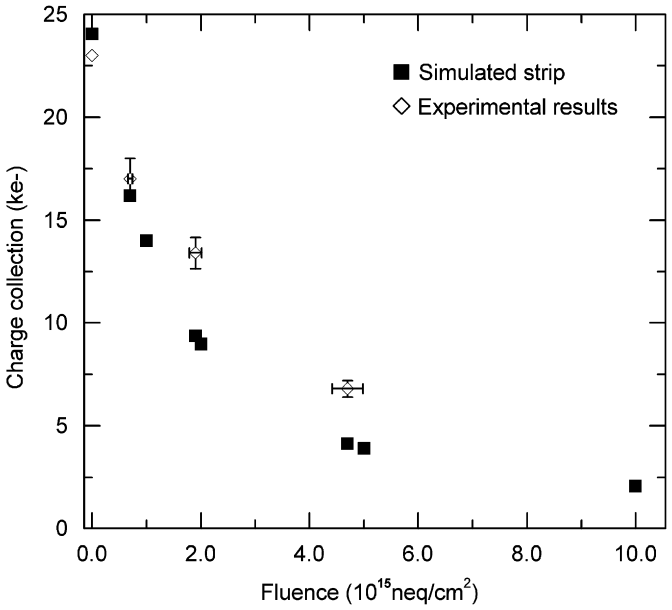

Fig. 2. Comparison between simulated and experimental charge collection in n-in-p strip detectors. Experimental results are taken from Ref. [22]. Both the simulation and the experimental results used 900 V bias.

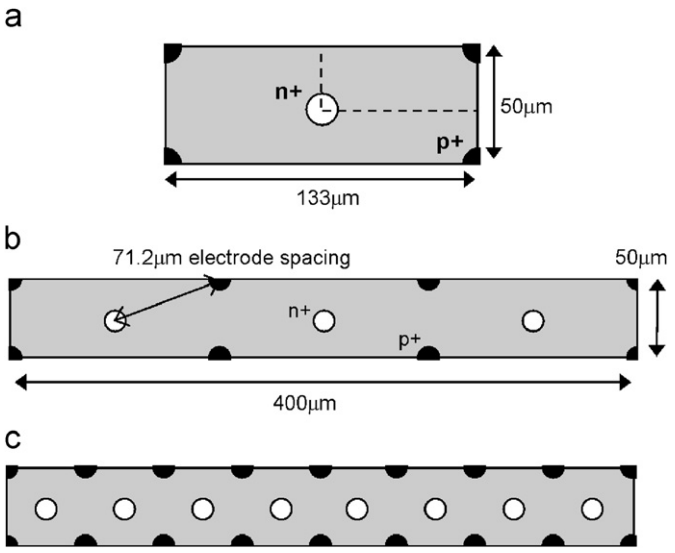

Fig. 3. 3D pixel layouts showing: (a) a simple sub-pixel with one n+ readout column, with the smallest repeating unit of the device being shown by a dotted line; (b) an ATLAS 3D pixel consisting of three of these simple sub-pixels, as used in Section 3; (c) an example of another ATLAS pixel layout using eight n+ readout columns.

starting a simulation with charge deposited along a track passing through the full thickness of the detector. The track generated 80 electron–hole pairs per micrometre, which is the most probable energy loss for a minimum ionising particle (MIP) passing through silicon, and its lateral profile was Gaussian with 1 μm standard deviation. The device's behaviour was simulated over time, and the current at the readout electrode was integrated over 10 ns, after subtracting the leakage current, to find the total charge collected. The simulation conditions were chosen to match the tests done in Ref. [22]—in particular, all the simulations were done at a high bias of 900 V.

The resulting charge collection results, in thousands of electrons, are shown in Fig. 2. The simulated CCE values follow the same trend as the experimental values. However, at higher fluences the simulations give substantially lower charge collection. This effect is also seen in other simulation work, such as Ref. [23].

Since experimental trapping rates are unavailable above $1 \times 10^{15}\,n_{eq}/cm^2$, the rates used in this simulation were extrapolated linearly from results at lower fluences. However, Ref. [18] provides some evidence that the trend in the trapping rate is less than linear at high fluences. So, it is likely that there is less carrier trapping at high fluences than this model predicts. The simulated CCE values here should be regarded as a pessimistic estimate.

3. Initial simulation of charge collection in an ATLAS 3D detector

In a simple 3D device with square pixels, each pixel would have a single readout electrode at its centre, and the bias electrodes would be placed at the corners of the pixels. However, the ATLAS pixel detector [3] uses a very elongated pixel size of 400 μm by 50 μm, which makes it possible to use a variety of different layouts, as illustrated in Fig. 3. Each ATLAS pixel can contain several n+ readout electrodes, which are shorted together. Each n+ electrode is then surrounded by p+ bias electrodes, so that the large ATLAS pixel is made up of a series of smaller sub-pixels. The number of n+ columns per pixel can be varied from 2 to 8, altering the spacing between the electrodes. The ATLAS pixel readout chip is specifically designed to use n+ readout rather than p+. Ref. [24] presents recent experimental charge collection results from a 3D ATLAS pixel detector with three n+ columns per pixel.

As mentioned previously, it is possible to simplify the device mesh, and hence speed up the simulation, by taking advantage of the pixel's symmetry. The mesh used here (Fig. 4) is sufficient for simulating depletion voltages, high-field behaviour, and charge collection, provided that we neglect charge sharing between adjacent pixels, which is relatively low in 3D detectors [25].

The experimental tests were done using an n-type substrate device with n+ readout electrodes. After irradiation with neutrons, the substrate type-inverted, becoming effectively p-type. These simulations, however, have been done using a p-type substrate and n+ readout. Since the radiation fluences used in these simulations are very high, the change in substrate type should not have much effect; the increase in the effective acceptor concentration produced by the traps will dominate over the initial substrate doping. Aside from this difference, the simulation mesh was closely matched to the real device. The details of the device structure were as follows:

- The substrate was 230 μm thick, with $7 \times 10^{11}\,cm^{-3}$ boron doping.

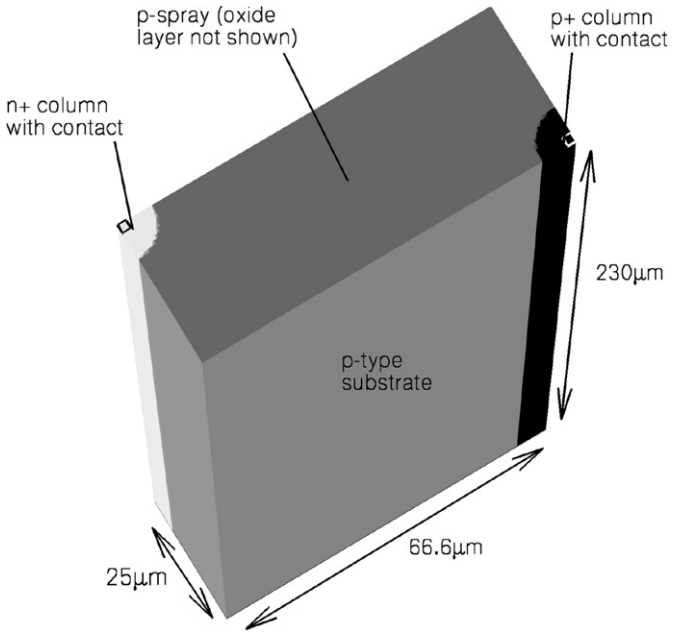

Fig. 4. Mesh used in the "3-column" ATLAS pixel detector simulations. The oxide layer is not shown.

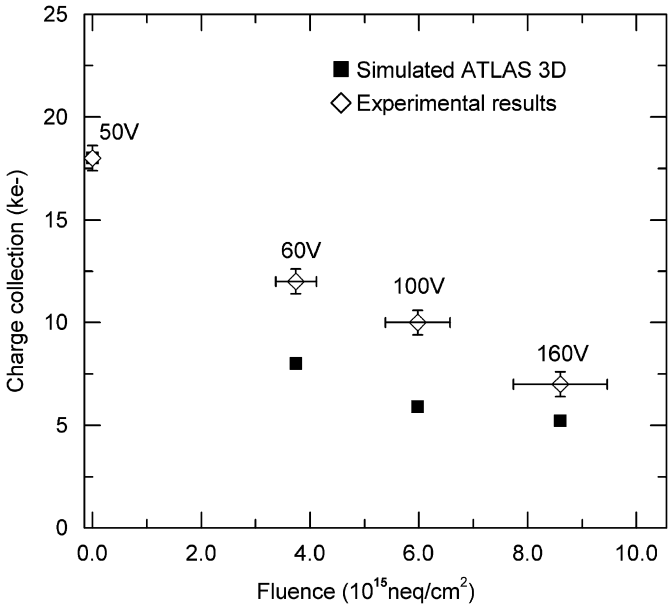

Fig. 5. Comparison between simulated and experimental charge collection in a "3-column" ATLAS pixel detector. Experimental results are taken from Ref. [24]. The labels indicate the bias used in both the experiments and the simulations.

- The columns were cylindrical and 5 µm in radius. The columns consisted of doped silicon, whereas polysilicon is used in real devices. The simulation used realistic doping profiles, which increased the radius of the p–n junction around the columns to about 6.5 µm.
- The n+ columns were isolated using a p-spray [26] covering the front and back surfaces. This used a total boron dose of $1.2 \times 10^{12}\,\mathrm{cm}^{-2}$, and had a peak concentration of $2.5 \times 10^{16}\,\mathrm{cm}^{-3}$. The p-spray was chosen to have a high enough dose to compensate for the electron layer (preventing it from linking the n+ columns together) and to have a fairly realistic profile.

This mesh was then used to do a series of charge collection simulations. The experimental tests [24] had been done using a de-focused, pulsed 1060 nm IR laser, which should provide fairly uniform charge deposition with depth. The resulting charge collection was then scaled to find the corresponding signal that would be produced by a MIP, which generates 80 electron–hole pairs per micrometre of silicon. In the test, a large number of pixels were connected together, which means charge sharing would have had no effect, and the current signals measured were averaged over 1000 pulses. To give an equivalent test of the average charge collection, the following simulations used uniform charge deposition throughout the device. Once again, the charge density was chosen to match a MIP, giving a total of about 18 500 electron–hole pairs. As before, the current signal was integrated over 10 ns, after correcting for the leakage current. Lastly, since the experimental tests were done using different biases at different fluences, the simulations also used varying biases. The charge collection results are shown in Fig. 5, and each data point is labelled with the corresponding bias voltage.

Once again, the simulation results show a similar trend to the experimental results, but give lower charge collection. The likely reasons for this have been discussed in Section 2.3. In the planar detector simulation (Fig. 2) the simulated collection efficiencies at high fluence are about 60–70% of the experimental values, and the same is true for the 3D detector, even though the two devices have very different structures. This indicates that these simulations can be useful for comparing and understanding the behaviour of different device structures.

4. Comprehensive simulation of 3D ATLAS pixel devices at $10^{16}\,n_{eq}/cm^2$ fluence

As mentioned in Section 3, a variety of different 3D ATLAS pixel layouts are possible, with the number of n+ electrodes per pixel ranging from 2 to 8—see Fig. 3 for examples of 3- and 8-column layouts. Using the same methods as described in the previous sections, all of these device layouts have been simulated in order to compare their performance at high fluence.

4.1. Depletion voltage and high-field behaviour

Using a fluence of $10^{16}\,n_{eq}/cm^2$, a steadily increasing bias was applied to each of the 3D structures until it reached full depletion. The resulting depletion voltages are shown in Fig. 6. In this figure, the x-axis gives the distance between the centres of neighbouring n+ and p+ electrodes, as shown in Fig. 3. Each data point is also labelled with the corresponding number of n+ columns per full ATLAS

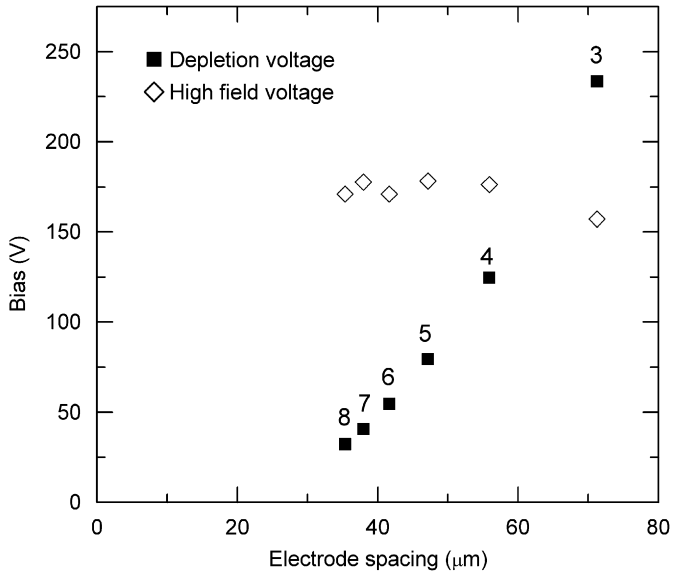

Fig. 6. Depletion voltage and high-field behaviour in ATLAS pixel devices at $10^{16}\,n_{eq}/cm^2$. The "high field voltage" refers to the voltage at which the maximum field in the device reaches 2.5×10^5 V/cm. The data points are labelled to show the number of n+ columns per pixel in each device.

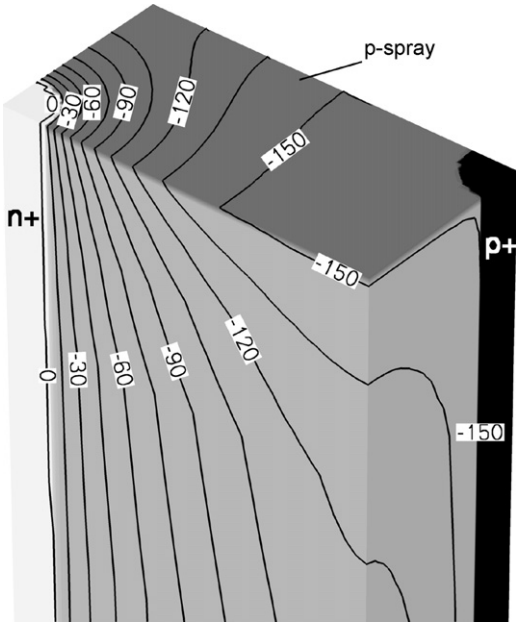

Fig. 7. Surface behaviour in a 4-column ATLAS pixel device at $10^{16}\,n_{eq}/cm^2$. The contour lines show the electrostatic potential, and shading indicates the doping. The n+ readout electrode is held at ground, and a bias of −150 V is applied to the p+ electrode. Notice how the bias applied to the p+ column also falls across the p-spray.

pixel. The result for the 2-column structure is omitted, because it is excessively high. It can be seen that the depletion voltage increases quadratically with the electrode spacing, with the devices with spacing of less than 40 μm being fully depleted at less than 50 V. In planar sensors, the full depletion voltage is also proportional to the square of the electrode spacing (i.e., the substrate thickness), which means that thick planar sensors cannot be fully depleted at this fluence.

Of course, although the devices with more widely spaced columns have higher depletion voltages, it might also be possible to apply a higher bias to them without breakdown occurring. To test this, these depletion voltage simulations also recorded how the maximum electric field within each device varied with the applied bias. This is not a precise measure of breakdown voltage, but it does give a reasonable indication of when the field is becoming dangerously high. Fig. 6 shows the point where the maximum field in each device reached 2.5×10^5 V/cm. The typical breakdown field in silicon is 3×10^5 V/cm. Somewhat surprisingly, this point is reached around 170 V in all of the devices, regardless of electrode spacing.

Looking at the results of the simulations in more detail, it becomes clear that surface effects have a major influence on the maximum field. As can be seen in Fig. 4, the p-spray makes contact with both the n+ and p+ electrodes. As a result, the bias applied to the p+ column is also applied to the p-spray, resulting in a high potential gradient where the p-spray meets the n+ column. This can be seen in Fig. 7, which shows the electrostatic potential in the 4-column ATLAS 3D device, using a fluence of $10^{16}\,n_{eq}/cm^2$ and a bias of 150 V. Ultimately, this means that the behaviour of the high-field region around the n+ column is much the same regardless of how far away the p+ columns are. In 3D detectors with p+ column readout and no isolation, a comparable effect is seen; the layer of electrons at the oxide interface makes contact with both sets of columns, the bias on the n+ columns is also applied to the electron layer, and so a high-field region develops where the electron layer meets the p+ column [9].

When the simulation was repeated for the 5-column ATLAS detector with no radiation damage, the "high-field voltage" was reduced dramatically, to just over 50 V. Ref. [24] also reports that an unirradiated ATLAS 3D sensor could not be biased far beyond 50 V. This effect is typical for p-spray isolation. After irradiation, the oxide charge is increased, and the electrons attracted by the oxide charge tend to compensate for the p-spray doping, reducing the maximum field [27]. Similarly, when the p-spray dose was doubled from 1.2×10^{12} to $2.4 \times 10^{12}\,cm^{-2}$, the electric field between the n+ column and the p-spray increased substantially.

Overall, these results show that using a larger number of columns—at least four per pixel—will allow the 3D devices to be fully depleted at very high fluences without the electric field becoming excessively large. More broadly, since the operating voltage is limited by the high-field region at the edge of the n+ column, it may be possible to improve the breakdown behaviour by altering the isolation. A field plate around the edge of the n+ column might reduce the maximum field at this point. Moderated p-spray, which acts like a combination of low-dose p-spray plus a p-stop, gives improved breakdown voltages in planar sensors [27]. When moderated p-spray is used,

after high irradiation the low-dose p-spray does not fully compensate the electron layer, and the high-field region shifts to the edge of the higher-dose p region. In a 3D detector, this effect could be particularly useful; we will no longer have an uninterrupted p-type layer linking the n+ and p+ electrodes, and the breakdown region will appear at a greater radius from the column, where the field will be lower due to the cylindrical geometry. More ambitiously, guard-ring-like structures might give a more gradual drop in potential across the surface between the n+ and p+ columns, particularly in devices with a larger column spacing.

4.2. Average charge collection efficiency at 10^{16} n_{eq}/cm^2

The previous section established that 150 V is a reasonable choice of bias for all the different 3D ATLAS devices. So, a series of charge collection simulations were done at 10^{16} n_{eq}/cm^2, using the same methods as in Section 3. Fig. 8 shows that the average collection efficiency increases as the electrode spacing is reduced. This is due to the decreasing collection distance, and the increasing electric field strength. The improvement is substantial, with the charge collected almost doubling as the number of columns per pixel is increased from 3 to 5. The "error bars" in this figure give an estimate of the variation in the collection efficiency with position, for the devices with 8, 6, 4 and 3 n+ columns per pixel, as described in Section 4.3. Devices with a small number of n+ columns show poorer uniformity, relative to the average collection.

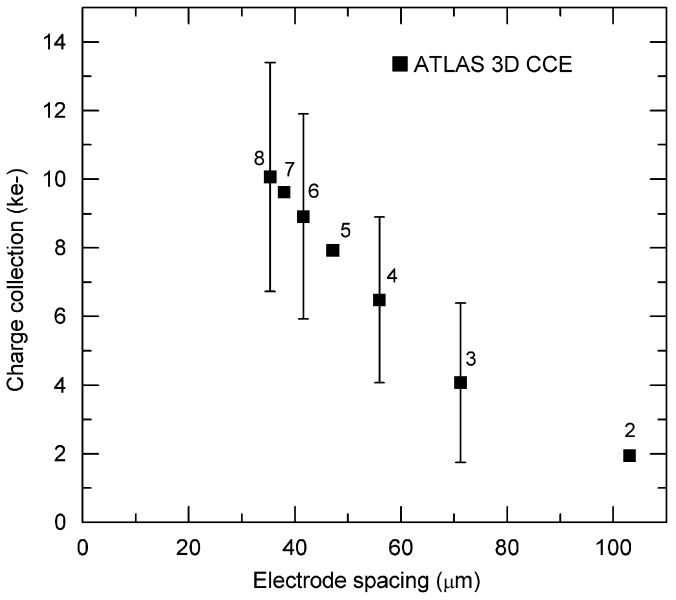

Fig. 8. Charge collection in different ATLAS pixel layouts at 10^{16} n_{eq}/cm^2 fluence. The data points give the average collection efficiency, and the "error bars" give an estimate of the variation in the charge collection with lateral position—see Section 4.3. This variation was only calculated for the 8-, 6-, 4- and 3-column devices. The applied bias was 150 V in all cases, and the charge deposited was 80 electron–hole pairs per micron.

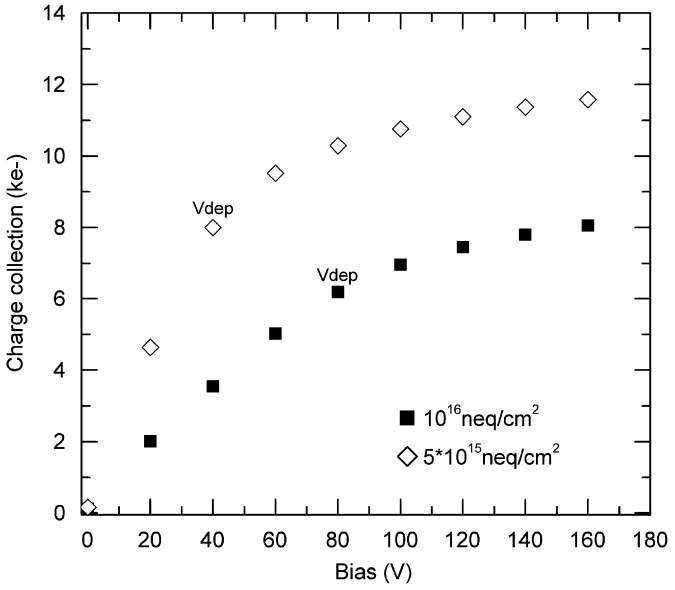

Fig. 9. Average charge collection in the 5-column ATLAS 3D detector against bias at two different fluences. The depletion voltages obtained from earlier simulations are indicated.

Additionally, Fig. 9 gives an example of how the charge collection in the 5-column ATLAS 3D device varies with the applied bias, with the results being shown at both 10^{16} n_{eq}/cm^2 and 5×10^{15} n_{eq}/cm^2. There is a clear change in the gradient of the curves when the depletion voltage is reached, although the charge collection continues to rise as the device is overbiased, due to the increasing electric field. This once again shows the benefits of choosing a device with more columns, in order to reduce the depletion voltage.

The effectiveness of a detector will depend on the amount of noise as well as the collection efficiency. This is considered in Section 4.4.

4.3. Uniformity of the charge collection across the pixel

Using a 3D detector structure means that the electric field and the carrier drift distances vary with the horizontal position across each pixel, rather than with depth. As a result, the charge collection efficiency may vary with horizontal position, too. The significance of this effect will vary depending on how the detector is used; if all the tracks are travelling parallel to the electrode columns, the effect will be particularly important.

Firstly, there is the effect of the electrode columns themselves. As shown in Ref. [28], the collection efficiency is substantially reduced within the columns, due to the lack of an electric field. As the number of columns per cell increases, the total area they occupy will obviously increase. The columns in these simulations are 5 μm in radius, with a doping profile extending a further 1.5 μm, which is the smallest radius that can currently be achieved with 230 μm columns. With these conditions, the columns will occupy 5% of the device volume in the 4-electrode

device, and 10% if eight n+ electrodes per pixel are used. If the radius of the columns is increased by just 2 μm, their total area will be doubled. Furthermore, unlike some of the other effects (e.g., trapping, increasing N_{eff}), the column area will reduce the device's effectiveness even before irradiation. So, although the average collected signal at 10^{16} n_{eq}/cm^2 steadily increases as more columns are used, it may be better to use a device with a lower average CCE and a smaller column area.

Secondly, Fig. 10 shows the electric field distributions in the 6-, 4- and 3-column ATLAS 3D devices, taken from horizontal cross-sections. Once again, the safe operating voltage of 150 V was used. All the devices show weaker electric fields towards the null points which occur at the "corners" of the mesh, midway between the n+ columns in neighbouring subpixels. Additionally, as the electrode spacing increases, the field becomes less uniform along the length of the pixel; in the 4-column device the field is distinctly weaker towards the p+ column, and the 3-column device is not fully depleted around the p+. This effect is due to the increase in the full depletion voltage.

The variation in the collection efficiency was studied by simulating the effects of MIPs passing through the detectors in different places. Because this was time-consuming to simulate, only the 8-, 6-, 4- and 3-column devices were considered. Each MIP passed vertically through the device, generating 80 e–h pairs/μm. The tracks had a Gaussian lateral distribution, with a standard deviation of 1 μm. These MIPs were simulated at 25 different positions in each detector structure, forming a regularly spaced 5×5 rectangular grid. Looking at the X- and Y-axes in Fig. 10, the first MIP was deposited at (2.5 μm, 2.5 μm), falling within the n+ column, and the final MIP deposited at the equivalent position within the p+ column. As before, these simulations were done at 10^{16} n_{eq}/cm^2, with 150 V bias. Note that this simulation did not consider the effects of charge sharing at the very edges of each pixel.

For each structure, the charge collection values from the 25 MIPs were averaged. These average values were close to the results obtained earlier in Section 4.2, with the biggest difference being 6%. So, this shows that while the 5×5 pattern does not map the collection efficiency with great resolution, the results are still reasonably representative of each device's behaviour. Next, the standard deviation of each set of MIP results was calculated, as a measure of the variation in collection efficiency with position. The standard deviation is shown in Fig. 8 by the "error bars". Relative to the average CCE, the standard deviation is larger in the devices with fewer n+ columns.

Fig. 11 shows the charge collection with position for the 4-column ATLAS 3D detector as an example. In all of

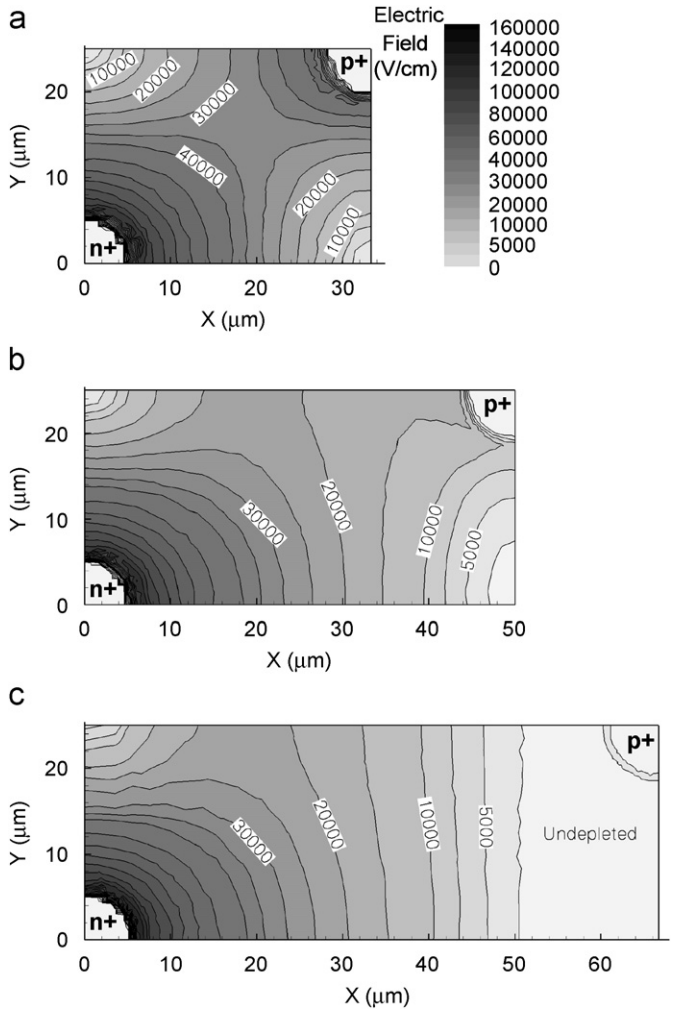

Fig. 10. Electric field distributions in ATLAS 3D devices with: (a) six columns per pixel; (b) four columns; (c) three columns. In each case the radiation fluence is 10^{16} n_{eq}/cm^2 and the bias is 150 V. The cross-sections are taken from the $z = 115$ μm plane, midway through the thickness of the substrate.

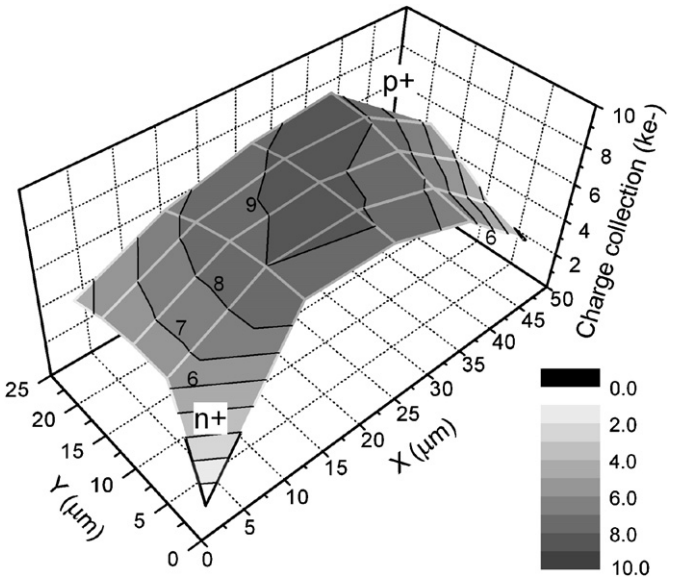

Fig. 11. Charge collection with position in a 4-column ATLAS 3D detector at 10^{16} n_{eq}/cm^2 and 150 V bias. The collection is indicated by both contours and height, and the grey lines show the positions of the 25 MIP simulations. Both the n+ and p+ columns show low sensitivity.

these ATLAS devices, negligible charge is collected when the MIP falls within the n+ or p+ column, as expected. (This confirms that the average collection simulated earlier includes the effects of the columns.) Aside from the columns, the lowest collection efficiencies are seen around the null points, as mentioned earlier, and to some extent around the edges of the cell—particularly the short edges in the devices with fewer columns. Generally, the highest collection signals are seen somewhere midway between the n+ and p+ columns. In most of the devices, the collection behaviour is somewhat more uniform than the electric field itself—for example, the 4-column device has a distinctly lower field near the p+ column than near the n+ (Fig. 10b) but there is not much difference in the collected signal from these two regions (Fig. 11). However, the 3-column device shows very poor collection around the p+ column, because this region is not fully depleted.

4.4. Capacitance and noise

Next, the capacitances of the ATLAS 3D structures were simulated. While the previous simulations used a relatively small region of the device, so that the charge collection simulations would be faster, the capacitance simulations were done using larger meshes. This meant that the C–V simulations were able to find the capacitance between the n+ readout columns and the p+ bias columns, and also the interpixel capacitance between one set of n+ columns and those in the two neighbouring pixels. Because ATLAS pixels are so elongated, the interpixel capacitance is much greater between pixels sharing their 400 μm-long sides than those sharing their 50 μm-long sides. The simulation does not account for the effects of the n+ and p+ columns in further-away pixels, but these effects should be fairly small. These capacitance simulations were done using saturated surface charge, but no bulk damage, because the capacitance simulations become unreliable when combined with trap modelling. A frequency of 1 MHz and a bias of 150 V were used.

Fig. 12 shows the total readout capacitance seen at each pixel, and also the capacitance between two neighbouring pixels. The total capacitance increases dramatically as the number of columns is increased, e.g., from 265 fF/pixel in the 4-column device to 580 fF/pixel with eight columns. This increase occurs not only because there are more n+ columns per pixel to contribute to the capacitance, but also because the capacitance seen at each individual column rises as the n+ and p+ columns become closer together.

For a pixel detector to operate, the collected charge signal must be large enough to exceed the readout chip's threshold. However, it is also important to be able to reliably distinguish genuine hits from noise. The readout noise of a detector increases with its capacitance, so although using a greater number of columns improves the devices' average collection efficiency, the increasing noise may counteract this. Tests of unirradiated ATLAS detectors show a linear increase in noise with capacitance

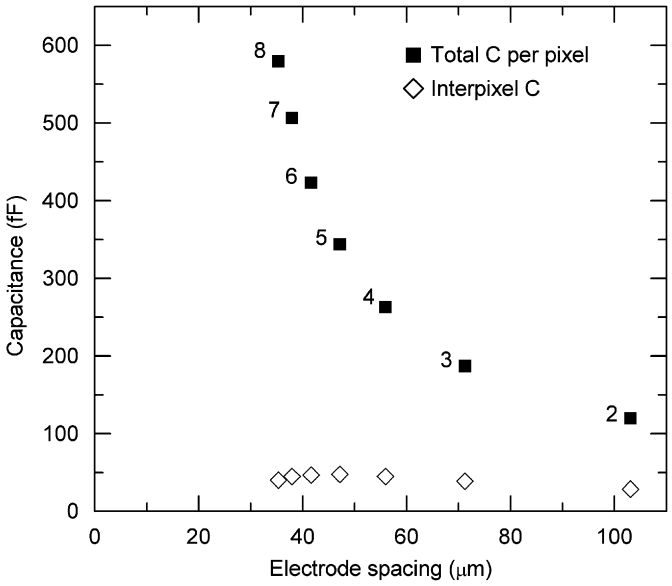

Fig. 12. Capacitance per pixel and interpixel capacitance in ATLAS 3D devices. No bulk damage was included in these simulations.

[29], with noise (electrons) $\simeq 60e^- + 39e^- \cdot (C/100\,\mathrm{fF})$. Ref. [30] reports that the noise in a typical ATLAS module increases only by 15% after irradiation to $10^{15}\,n_{eq}/cm^2$, provided that it is cooled to reduce leakage current, so the relationship above was taken as an acceptable estimate of the noise in an irradiated ATLAS 3D sensor. The noise was calculated for each ATLAS layout, assuming that the preamplifier and stray capacitances contribute an extra 100 fF, then added in quadrature with a threshold dispersion of $70e^-$. Then, the signal-to-noise ratios in these detectors were estimated by combining these values with the average collection efficiencies at $10^{16}\,n_{eq}/cm^2$. The results are shown in Fig. 13. Although the signal-to-noise ratio increases substantially going from the 3-column to the 5-column device, increasing the number of columns further does not improve the SNR, which actually falls slightly when using eight columns.

The interpixel capacitance in Fig. 12 is an order of magnitude smaller than the total capacitance, and does not increase very much as the number of columns is increased. Unsurprisingly, the capacitance between adjacent n+ and p+ columns dominates the total capacitance. In contrast, the n+ and p+ contacts in a planar detector are separated by 300 μm or so of silicon, and the interpixel capacitance tends to dominate.

The capacitance simulations were repeated using no p-spray and no oxide charge, to see how the devices would behave when surface effects were eliminated. The readout capacitance was reduced by 10% or less in each device at 150 V. The surface effects made a larger contribution to the capacitance at lower biases—for example, at 10 V there was a 20% difference in capacitance. Overall, the surface causes some coupling between the n+ and p+ columns, but the effect is relatively small.

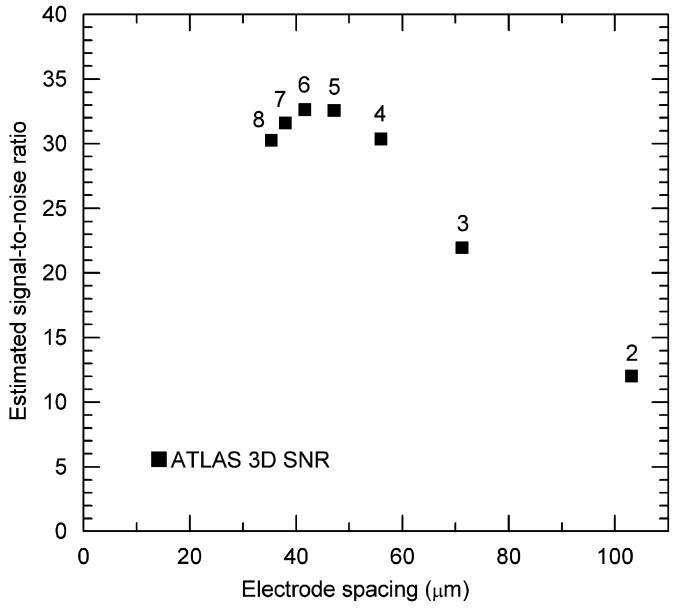

Fig. 13. Estimated signal-to-noise ratio in ATLAS 3D detectors after 10^{16} n_{eq}/cm^2 irradiation, based on previous CCE and capacitance simulations.

5. Conclusions

These simulations have modelled the behaviour of different 3D detectors at Super-LHC radiation-damage levels. Overall, the simulations show improved depletion and charge collection behaviour compared to planar detectors. Comparisons between different ATLAS 3D pixel layouts have shown that if the number of n+ electrodes per pixel is small, the wide electrode spacing means that the depletion voltage, the average collection efficiency and the uniformity of the collection across the pixel are poorer. The surface effects which can cause breakdown are not strongly affected by the electrode spacing. Getting an acceptable depletion voltage and uniformity at high fluence requires at least four columns per pixel. Conversely, using a large number of columns per pixel will mean that the columns themselves will take up a significant proportion of the device volume (particularly if the columns have a greater radius than the 5 μm used here), and the rapidly increasing capacitive noise limits the signal-to-noise ratio. The improvements in the absolute charge collection and depletion voltage obtained by using more than six columns are relatively small. So, for detectors operating at 10^{16} n_{eq}/cm^2, the best trade-off is likely to be achieved by using 4–6 columns.

Currently, groups within the CERN RD50 collaboration and the ATLAS 3D sensors project are producing a variety of 3D devices. These simulations should complement these experimental tests, by highlighting potential problems with the devices such as high capacitance or nonuniformity in collection, and by aiding the understanding of these devices' behaviour.

References

[1] J. Ellis, Eur. Phys. J. C 34 (1) (2004) 51.
[2] F. Gianotti, Nucl. Phys. B—Proc. Suppl. 147 (2005) 23.
[3] G. Gagliardi, Nucl. Instr. and Meth. A 546 (1–2) (2005) 67.
[4] Y. Unno, Nucl. Instr. and Meth. A 569 (1) (2006) 41.
[5] S.I. Parker, C.J. Kenney, J. Segal, Nucl. Instr. and Meth. A 395 (3) (1997) 328.
[6] C. Da Via, G. Anelli, J. Hasi, P. Jarron, C. Kenney, A. Kok, S. Parker, E. Perozziello, S.J. Watts, Nucl. Instr. and Meth. A 509 (1–3) (2003) 86.
[7] M. Moll, on behalf of the RD50 Collaboration, Nucl. Instr. and Meth. A 565 (1) (2006) 202.
[8] J. Kalliopuska, S. Eranen, R. Orava, Nucl. Instr. and Meth. A 572 (1) (2007) 292.
[9] D. Pennicard, G. Pellegrini, M. Lozano, R. Bates, C. Parkes, V. O'Shea, V. Wright, IEEE Trans. Nucl. Sci. NS-54 (4) (2007) 1435.
[10] Synopsys Inc., Synopsys TCAD manuals ⟨http://www.synopsys.com/products/tcad/tcad.html⟩, 2007.
[11] G. Lutz, Semiconductor Radiation Detectors Device Physics, first ed., Springer, Berlin, Heidelberg, New York, 1999.
[12] J. Kalliopuska, S. Eranen, R. Orava, Nucl. Instr. and Meth. A 568 (1) (2006) 27.
[13] R.H. Richter, L. Andricek, T. Gebhart, D. Hauff, J. Kemmer, G. Lutz, R. Weiss, A. Rolf, Nucl. Instr. and Meth. A 377 (2–3) (1996) 412.
[14] V. Eremin, E. Verbitskaya, Z. Li, Nucl. Instr. and Meth. A 476 (3) (2002) 537.
[15] W. Shockley, W.T. Read, Phys. Rev. 87 (5) (1952) 835.
[16] M. Petasecca, F. Moscatelli, D. Passeri, G.U. Pignatel, IEEE Trans. Nucl. Sci. NS-53 (5) (2006) 2971.
[17] G. Kramberger, V. Cindro, I. Mandic, M. Mikuz, M. Zavrtanik, Nucl. Instr. and Meth. A 481 (1–3) (2002) 297.
[18] V. Cindro, G. Kramberger, M. Lozano, I. Mandic, M. Mikuz, G. Pellegrini, J. Pulko, M. Ullan, M. Zavrtanik, IEEE Nucl. Sci. Symp. Conf. Rec. 1 (2006) 139.
[19] J.W. Slotboom, H.C. Degraaff, Solid-State Electron. 19 (10) (1976) 857.
[20] M. Lozano, G. Pellegrini, C. Fleta, C. Loderer, J.M. Rafi, M. Ullan, F. Campabadal, C. Martinez, M. Key, G. Casse, P. Allport, IEEE Trans. Nucl. Sci. NS-52 (5) (2005) 1468.
[21] M. Moll, Radiation damage in silicon particle detectors—microscopic defects and macroscopic properties, Thesis/Dissertation, Hamburg, 1999.
[22] P.P. Allport, G. Casse, M. Lozano, P. Sutcliffe, J.J. Velthuis, J. Vossebeld, IEEE Trans. Nucl. Sci. NS-52 (5) (2005) 1903.
[23] G. Kramberger, V. Cindro, I. Mandic, M. Mikuz, Nucl. Instr. and Meth. A 579 (2) (2007) 762.
[24] C. Da Via, J. Hasi, C. Kenney, V. Linhart, S. Parker, T. Slavicek, S.J. Watts, P. Bem, T. Horadzofski, S. Pospisil, Nucl. Instr. and Meth. A 587 (2–3) (2008) 243.
[25] V.A. Wright, W.D. Davidson, J.J. Melone, V. O'Shea, K.M. Smith, L. Donohue, L. Lea, K. Robb, S. Nenonen, H. Sipila, IEEE Trans. Nucl. Sci. NS-52 (5) (2005) 1873.
[26] G. Pellegrini, C. Fleta, F. Campabadal, S. Diez, M. Lozano, J.M. Rafi, M. Ullan, Nucl. Instr. and Meth. A 566 (2) (2006) 360.
[27] C. Piemonte, IEEE Trans. Nucl. Sci. NS-53 (3) (2006) 1694.
[28] A. Kok, Signal formation and active edge studies of 3D silicon detector technology, Thesis/Dissertation, Brunel University, 2005.
[29] A. Andreazza, Nucl. Instr. and Meth. A 461 (1–3) (2001) 168.
[30] J. Grosse-Knetter, Nucl. Instr. and Meth. A 568 (1) (2006) 252.